On the preparation of multifunctional conversion coatings of FePO 4 /LiFePO 4

S. Valverde-Pérez, R. Figueroa, X.R. Nóvoa, D.S. Ramírez-Rico, Vincent Vivier

On the preparation of multifunctional conversion coatings of $FePO_4$/$LiFePO_4$.

S. Valverde-Pérez[1], R. Figueroa[1], X.R. Nóvoa[1]*, D. S. Ramírez-Rico[2], V. Vivier[2]

[1]CINTECX, Universidade de Vigo, EEI, ENCOMAT Group, 36310 Vigo, Spain.

[2]Sorbonne Université, CNRS, Laboratoire de Réactivité de Surface (LRS), 4 Place Jussieu, F-75005 Paris, France.

*Corresponding author: rnovoa@uvigo.es (Ramón Nóvoa)

Abstract

This research aims to take advantage of the properties of phosphate coatings to overcome the problems inherent in using $LiFePO_4$ as a powder. $LiFePO_4$ coatings have been prepared on iron sheets using cyclic voltammetry in an aqueous solution of H_3PO_4 and LiOH. The voltammograms evolved from the initial active-passive behaviour, typical for iron in H_3PO_4 solution, to a reversible redox behaviour upon cycling. The resulting coating was characterised morphologically (via SEM and optical microscopies), chemically (via XPS) and electrochemically (via EIS and SECM). The results showed a two-layered coating (a porous outer layer and a compact inner layer) with the behaviour of a porous electrode that reversibly exchanges Li^+ ions with the environment and reduces the emission of ionic species (Fe^{2+}, Fe^{3+}) as its thickness increases.

1. Introduction

Phosphate coatings have a long tradition as treatments to increase the corrosion resistance of metallic substrates, improve the adhesion of organic coatings, or increase the wear resistance. Metallic substrates such as plain carbon steel, galvanized steel, stainless steel, and Mg or Al alloys, are protected by conversion coatings usually grown by relatively simple, fast, and low-cost processes[1–6].

Furthermore, batteries based on $LiFePO_4$ (LFP) are nowadays the automotive industry's reference technology. LFP is a non-toxic, low-cost, safe and highly reversible material for positive electrodes [7,8]. The $LiFePO_4$ olivine structure as a suitable material for positive electrodes was recognised in 1997 [9], which makes LFP batteries a mature technology optimised by numerous researchers [10]. The theoretical capacity is 170 Ah/kg, the cyclic charge/discharge stability and the minimal capacity loss on cycling make $LiFePO_4$ interesting for commercial use [11–14]. In addition, the low electronic conductivity of the pure $LiFePO_4$ cathode is a drawback that has been overcome by focusing on particle size reduction or carbon doping [11,15,16].

Currently, the $LiFePO_4$ active material for Li-ion batteries (LIBs) is usually produced as a powder via chemical, mechanical, or hydrothermal routes [16–21] and increasing effort is put into recovering spent material [22]. Whatever the origin of the obtained powder, the preparation of the electrode requires the active material to be stuck on the Al current collector, which generates a contact resistance at the interface, which is not continuous due to the particulate nature of the active material. Although conductivity promoters such as graphite are added to the electrode material, it usually results in an uneven conductivity along the active material-current collector interface [23].

Thus, phosphates, especially iron phosphates, can play a multifunctional role depending on their physical form. As films, the primary function is anti-corrosion, whereas as powders, the relevant functionality is as an active material for LIBs. This research aims to combine both functionalities by developing a phosphate coating for energy applications. $LiFePO_4$ layers are grown by electrochemical methods on iron sheets that serve as current collectors, thus integrating the active material and the current collector in a single structure. This structure eliminates the issue of lack of conductivity between the active material and the current collector. We will show how the active material can be grown using the cyclic voltammetry technique in a solution of H_3PO_4 and LiOH.

2. Experimental methods

The electrochemical synthesis and characterisation were conducted using a potentiostat PGSTAT-302N (Metrohm-Autolab B.V.). A three-electrode cell was used for the synthesis procedure. The reference electrode was a saturated calomel electrode (SCE), the counter electrode was a platinum mesh, and the working electrode was a Fe^0 foil 99.5% (Goodfellow) with a 2 cm^2 nominal active surface defined by an O-ring. The synthesis solution was 2.85 M H_3PO_4 and 2.85 M LiOH (analytical grade reagents), resulting in ~32 $mS \cdot cm^{-1}$ conductivity. The control of pH is needed to avoid phase segregation, according to the Pourbaix diagram [24], and the pH of the solution was adjusted to 4±0.1 when necessary, dropwise, with 4 M LiOH. The only treatment performed on the Fe foil was degreasing with acetone, followed by methanol and rinsing with deionised water.

The electrochemical procedure was initiated with the sample's cathodic cleaning by setting the potential to -0.75 V vs SCE during 60 s. Afterwards, cyclic voltammetry (CV) was performed between -0.75 V to 1.4 V vs SCE at 5, 10, 15, and 20 mV/s scan rate. Up to 40 CV cycles were performed.

Additional electrochemical characterisation was performed by electrochemical impedance spectroscopy (EIS). This technique was used at the end of the synthesis, with the same three-electrode cell, allowing to study in situ the conversion layer. The frequency range was scanned from 100 kHz to 100 mHz with an amplitude of 10 mV rms and 7 points per decade at -0.7 V vs SCE polarisation potential. The cell geometry guarantees a constant distance between the working and reference electrode for all the experiments.

The morphology and chemical composition of the conversion layer was characterised as follows. A JEOL® 5410 from OXFORD instruments® scanning electron microscopy (SEM) was used to study the microstructure of the coating. A Link ISIS 300 EDS detector integrated in the SEM was employed to access the chemical composition. XPS ESCALAB 250iXL from ThermoFisher-Scientific was used to complete the chemical characterisation. The samples were washed with deionised water and dried in a warm air stream before examination.

The scanning electrochemical microscopy (SECM) technique was also employed to access additional information on the formed coatings. A Sensolytics SECM system coupled to a Bipotentiostat/Galvanostat PGSTAT30 (Methrom Autolab B.V.) was used in a four-electrode cell arrangement. The reference electrode was a saturated Ag/AgCl electrode, the counter electrode was a platinum mesh, the substrate working electrode was the prepared coating (with a small surface to minimise cross-coupling with the SECM tip[25,26]), and the SECM tip was a 10 µm diameter platinum microelectrode in the centre of a glass capillary of 100 µm diameter.

3. Results and discussion

3.1. Synthesis

The physicochemical properties of the electrolyte are critical in the synthesis process. No effective passivation was obtained upon potential scan for solution conductivity lower than 32 mS cm^{-1}. Moreover, according to thermodynamics, although the pH window for $LiFePO_4$ formation is between 3 and 8 [24], for pH >4.1, precipitation occurs. Hence the synthesis solution was maintained at pH= 4 ±0.1. All the solutions were kept open to the air, unstirred, and at room temperature (~20 °C).

Figure 1 shows typical first CV curves. The forward record follows the trend reported for iron in phosphoric acid [27]; a sudden current drop occurs once the potential reaches the passivation potential value. Moreover, for sweep rates higher than 5 mV s^{-1}, the passivation potential increases with the sweep rate, revealing an ohmic-type control of the process [28]. The CV behaviour for the scan performed at 5 mV s^{-1} scan rate (Fig. 1) is different than for the other scan

rates because, under the conditions of the experiment (quiescent solution), the coating does not reach a homogeneous growth over the entire surface. This aspect will be discussed later.

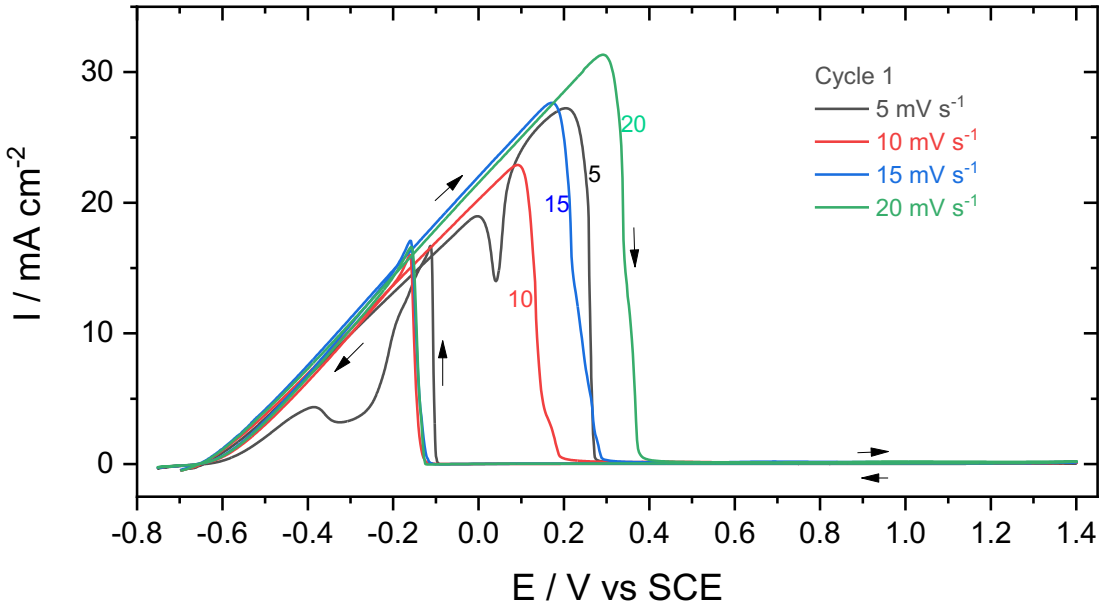

Figure 1. Fe electrode in 2.85 M H_3PO_4 and 2.85 M LiOH electrolyte. First cycle of the CV in the synthesis process for various scan rates.

Interestingly, for the scan rates higher than 5 mV s^{-1}, the surface reactivation potentials (Flade potential) are identical, and the reverse curves superimpose, showing that a single species is responsible for the passivation, no matter the scan rate. Further insight into this aspect was obtained by recording the evolution of the open circuit potential after stopping the potential sweep at 1 V/SCE, as shown in Fig. 2a after a different number of CV curves was performed at the 10 mV s^{-1} sweep rate. As expected, the electrode potential jumps from passive to active potential after a specific time depending on the number of CV curves performed. The transition potential is the Flade potential, that tends to -0.1 V/SCE, similarly to the results reported in Fig. 1 in the case of CV.

Moreover, Fig. 2a shows that the time to reach the Flade potential increases with the number of cycles during the first fourteen cycles. Afterwards, it oscillates between 1100 and 1600 s (inset in Fig. 2a). This behaviour can be understood assuming a coating thickening during the first cycles until reaching a steady state by the 15th cycle. Fig. 2b shows more clearly the reaching of the steady state, considering the exchanged charge during each cycle, which decreases until the 14th cycle and then remains constant, indicating the formation of a stable coating.

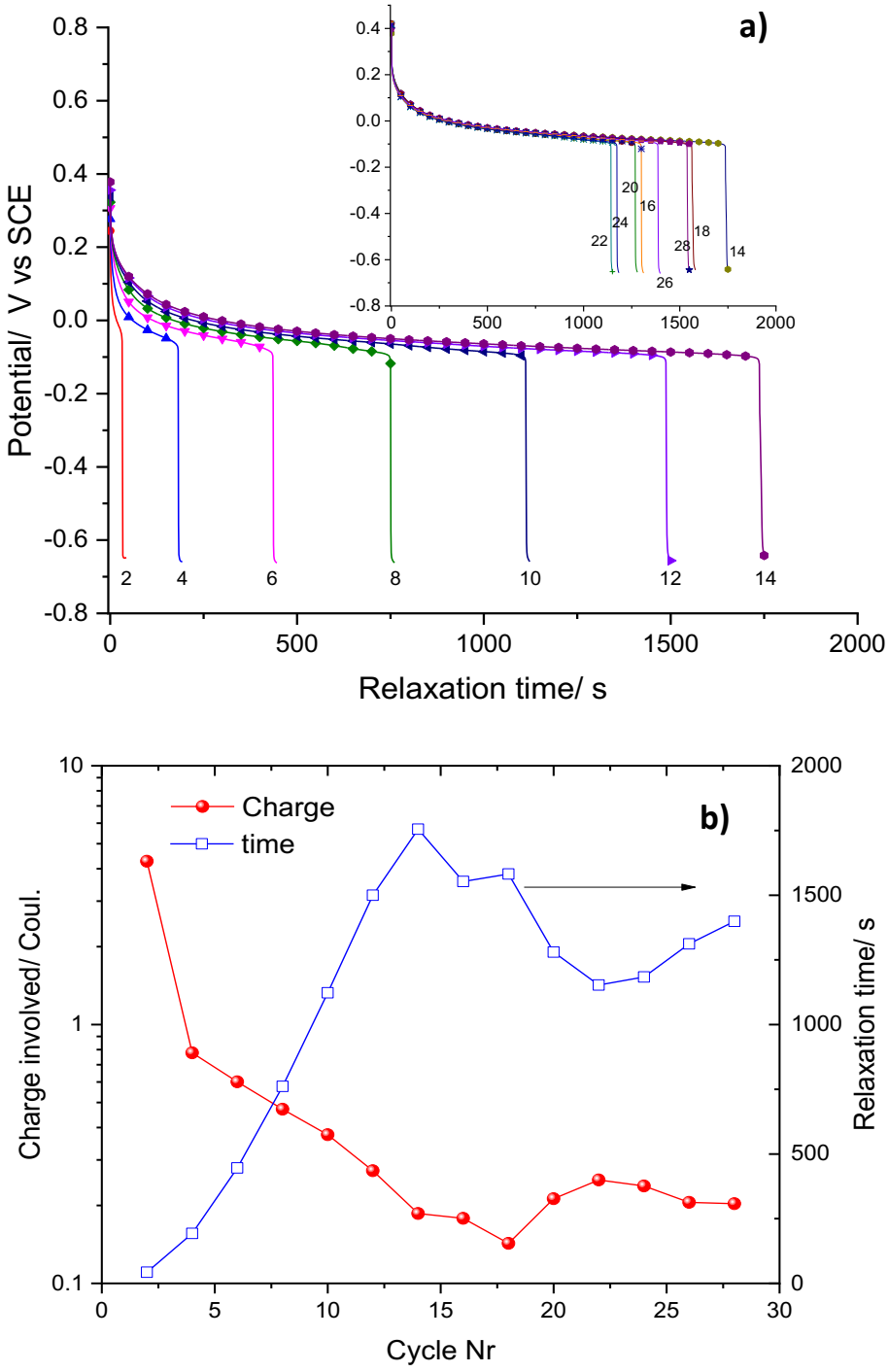

Figure 2. **a)** Evolution of the electrode open circuit potential after stopping sweep at 1 V/SCE in the forward scan (at 10 mV s^{-1})— labels correspond to the cycle number; the insert corresponds to cycles 14 to 28. **b)** Evolution of the relaxation times obtained from data presented in a), and the charge involved in the coating formation.

Interestingly, the shape of the first CV curves shown in Fig. 1 changes relatively rapidly upon cycling, and the presence of two current maxima observed at 5 mV s^{-1} (Fig 1) becomes more evident at all scan rates. The overall current decreases with the increasing number of cycles, as

illustrated in Fig. 3a. The activity domain has at least two maxima on both forward and backward scans.

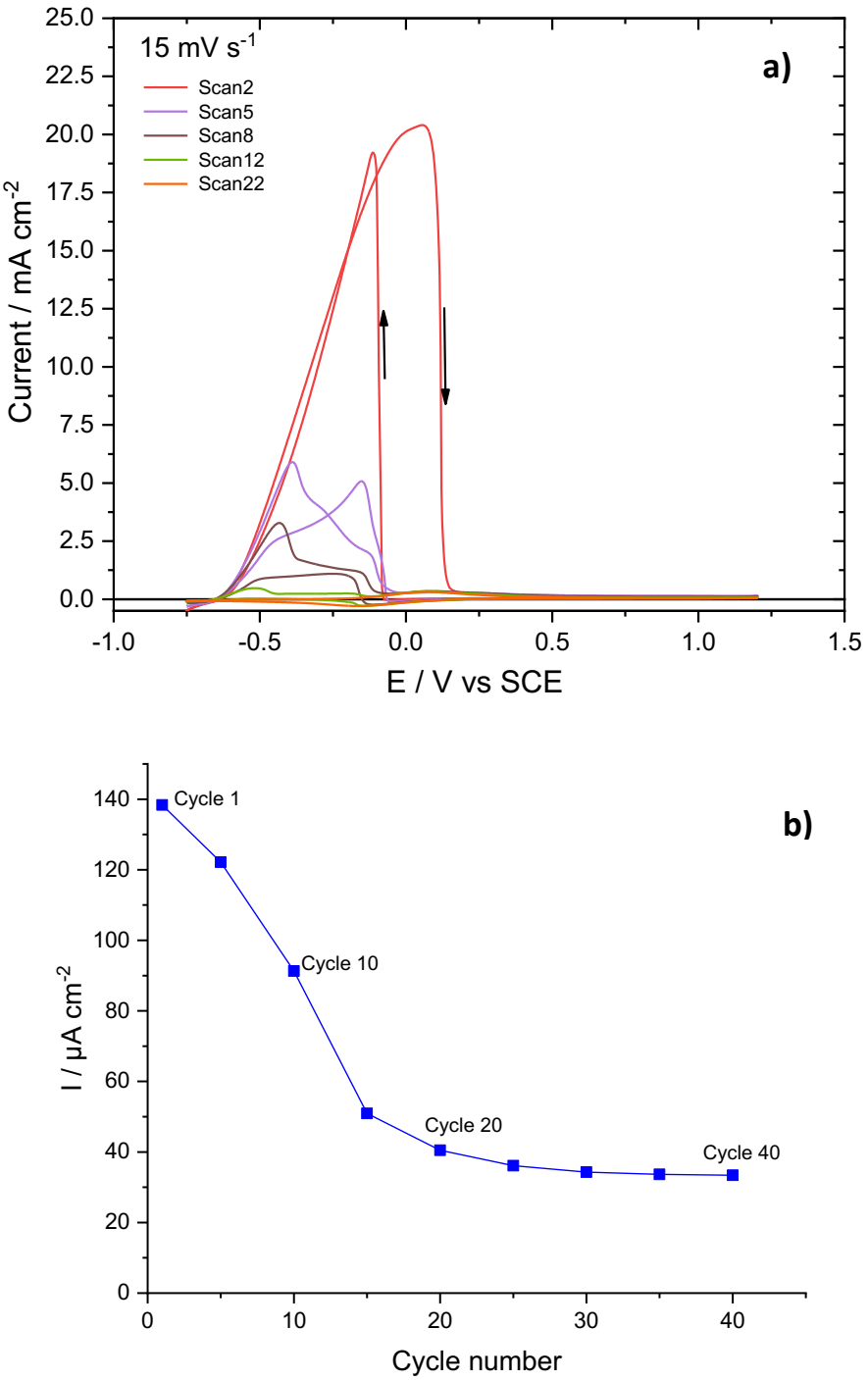

Figure 3. **a)** Successive CV curves at 15 mV s^{-1} of a Fe electrode in 2.85 M H_3PO_4 and 2.85 M LiOH electrolyte. **b)** Evolution of the current in the passive domain (measured at 1 V/SCE) as a function of the number of cycles.

Moreover, the current measured at 1 V/SCE in the passive domain decreases during the first 20 cycles, as shown in Fig. 3b, and then tends towards a steady state value after the 20th cycle. This

trend is similar to the one described for the charge variation presented in Fig. 2b. These two parameters point to the progressive formation of a stable coating upon cycling.

Figure 4 clearly shows that, from the 20th cycle and beyond, the structure undergoes a reversible redox reaction. For the 20th cycle, a tiny peak can be observed at about -0.5V/SCE, corresponding to the oxidation of the substrate ($Fe \longrightarrow Fe^{2+} + 2e^{-}$), but this disappeared from the 25th cycle onwards, and the active-passive transition has vanished in the voltammograms, which have progressively transformed into a reversible redox characteristic. Such a feature should correspond to insertion/deinsertion of Li^{+} in the phosphate layer associated with the Fe^{3+}/Fe^{2+} redox process. This explains the stabilisation in the current measured at 1 V/SCE (Fig. 3b). Coating thickness stops increasing as the incorporation of additional Fe^{2+} from substrate oxidation ceases, and redox activity corresponds to the electrochemical response of the coating formed during the first 20 cycles.

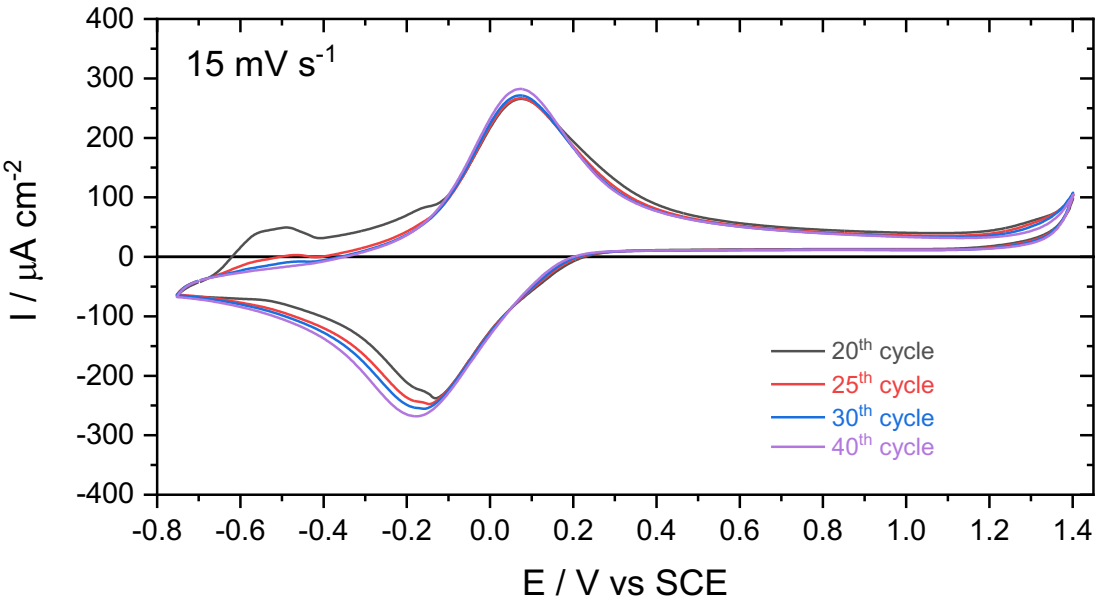

The

Figure 4. Cyclic voltammograms (cycles #20 to #40) recorded during the synthesis procedure at 15 mV s^{-1}.

3.2. Electrochemical Impedance Spectroscopy

EIS measurements were performed in situ during the finishing procedure at a given number of cycles to get information about the evolution of the properties of the coating. EIS spectra presented in Fig. 5a were obtained for a cycling at 10 mV s^{-1} after 5, 10, and 15 cycles. The low-frequency limit of the impedance increases with the cycle number, maintaining almost invariant the characteristic frequency, which can be related to the increase of the coating thickness.

The high frequency part of the Nyquist plots in Fig. 5a clearly shows a near 45° slope characteristic of a transmission line feature typical of porous electrodes. Moreover, the insert in Fig. 5a shows that the high-frequency limit varies with the number of cycles, which also points to the development of a conducting porous structure, for which the high-frequency limit is a function of the conductivity of the coating material and the coating thickness[29–31].

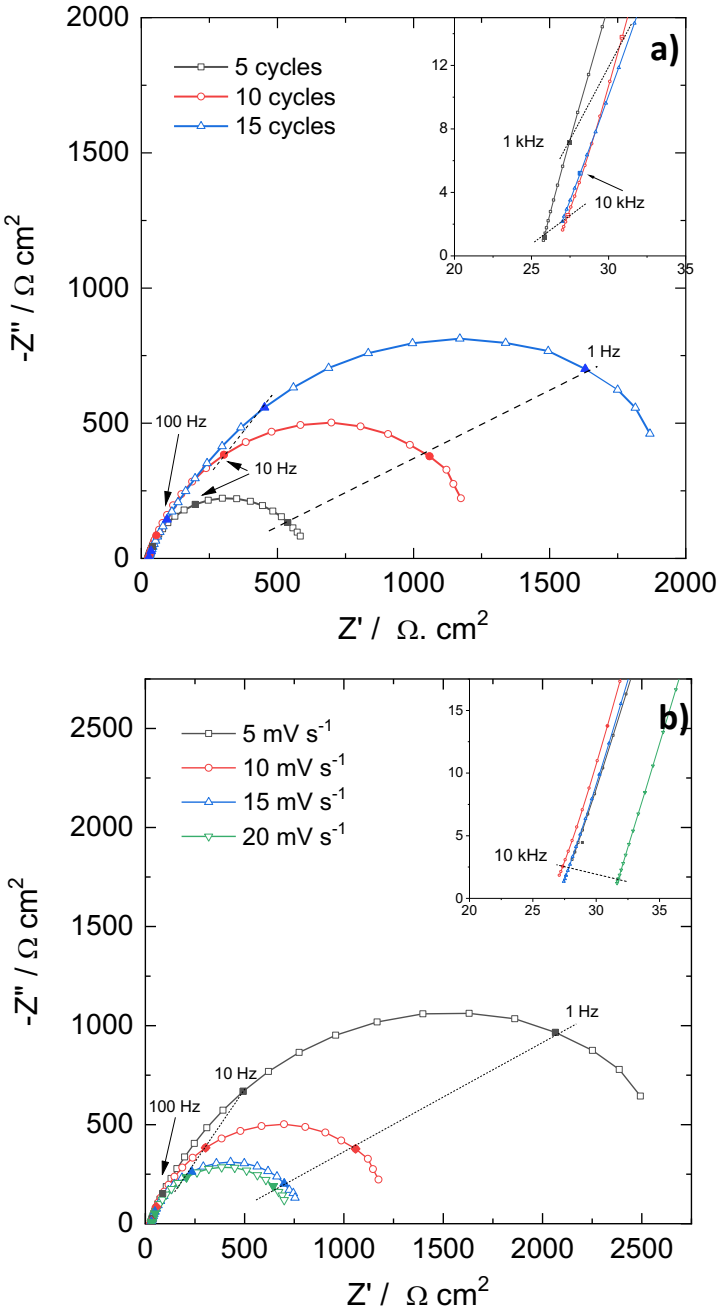

Figure 5. Nyquist impedance plots obtained in the synthesis solution at the open circuit potential. **a)** Effect of the number of cycles (at 10 mV s^{-1}). **b)** Effect of the scan rate (after 10 cycles).

Figure 5b summarises the effect of the scan rate for a fixed number of cycles (10 cycles). The low-frequency limit of the impedance decreases as the sweep rate increases, as can be expected

due to the decrease in the charge involved, which leads to the formation of a thinner coating. Moreover, the insert of Fig. 5b shows the shift in the high-frequency limit (porous electrode) increases with the sweep rate, which seems to affect the microstructure of the formed coating significantly. For a constant reference-to-working electrode distance and stable chemistry of the coating, the resistance associated with the ionic conduction is the most probable factor responsible for the observed shift, which is directly linked to the film pore structure. The supplementary information file presents a detailed description of the porous structure development in terms of electrical equivalent circuit parameters.

3.3. Scanning electron microscopy

Morphological and chemical characterisation using SEM confirm the EIS results: the coating is porous, and the surface porosity depends on the scan rate. Fig. 6a shows that, after 10 cycles, the coating is highly defective, covers only partially the surface (Fig. 6a1), and shows poor adhesion for 5 mV s^{-1}. For higher sweep rates (Figs. 6b, c, d and 6b1, c1, d1), the coatings are homogeneous, well adhered to the substrate, and porous. Both results obtained at 10 mV s^{-1} and 15 mV s^{-1} are adequate for a good film formation in terms of adhesion and porosity for the reversibility of the Li^+ insertion process [32].

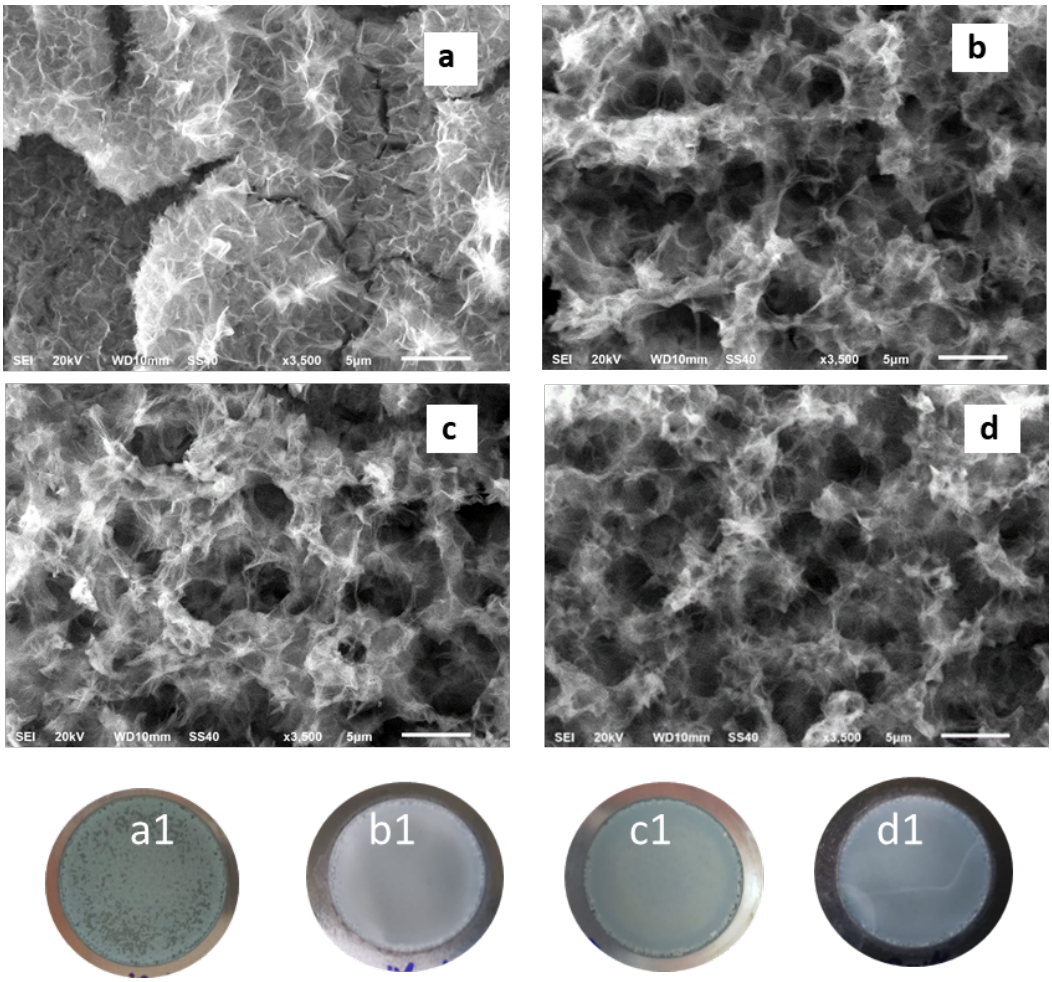

Figure 6. SEM images (**a** to **d**), and optical images (**a1** to **d1**) obtained after 10 cycles at 5 mV s^{-1} (**a**, and **a1**); 10 mV s^{-1} (**b**, and **b1**); 15 mV s^{-1} (**c**, and **c1**); and 20 mV s^{-1} (**d**, and **d1**).

The chemical composition of the coatings and the effect of the number of cycles is summarised in Fig. 7, which shows SEM images and corresponding EDX analysis of the electrode for a scan rate of 15 mV s^{-1} after 10 and 40 cycles. The porosity of the conversion layer decreases with the number of cycles, but the chemical composition remains unchanged with a Fe/P ratio lower than that ratio corresponding to the stoichiometry of $FePO_4$ (1:1). Although it is not clear the origin of the excess of P in the coating, the ratio Fe/P is invariant with the number of cycles (thickness), indicating the necessary presence of Fe^{2+} in the coating, which should be associated with Li^+ incorporation for charge balance, responsible of the redox feature shown in Fig. 4. Li^+ cannot be detected with EDX analysis. The presence of both Fe^{2+} and Fe^{3+} in the coating provides the electronic conductivity of the phosphate coating [33], which also explains the transmission line feature observed on the impedance spectra presented in Fig. 5 in the high-frequency domain.

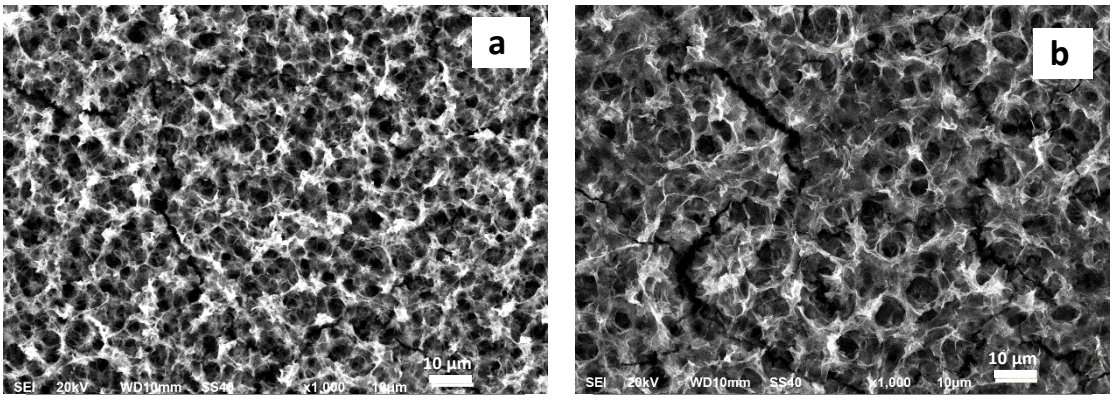

Element	Weight [%]	Atomic [%]
O	53.2	74.4
P	21.4	15.5
Fe	25.4	10.2

Element	Weight [%]	Atomic [%]
O	52.5	73.9
P	21.5	15.6
Fe	26.0	10.5

Figure 7. SEM images and corresponding EDX analysis of a coating synthesised at 15 mV s^{-1}: **a)** after 10 cycles; and **b)** after 40 cycles.

The porous nature of the coatings is well illustrated in Fig. 8, corresponding to the cross-section of a coating formed at 15 mV s^{-1} for 20 cycles. The average layer thickness is 26 µm and the porous structure extends over almost the entire thickness. Interestingly, a second thin region can be differentiated. In the upper part of the image, at the interface between the iron and the phosphate layer, a compact region of approximately 3-4 µm thick can be distinguished. Thus, the layer grows with high porosity, offering an ample active area for Li^+ insertion/deinsertion into the phosphate structure and maintaining a compact morphology at the metallic substrate interface. This aspect is relevant for the discussion in the SECM section (vide infra).

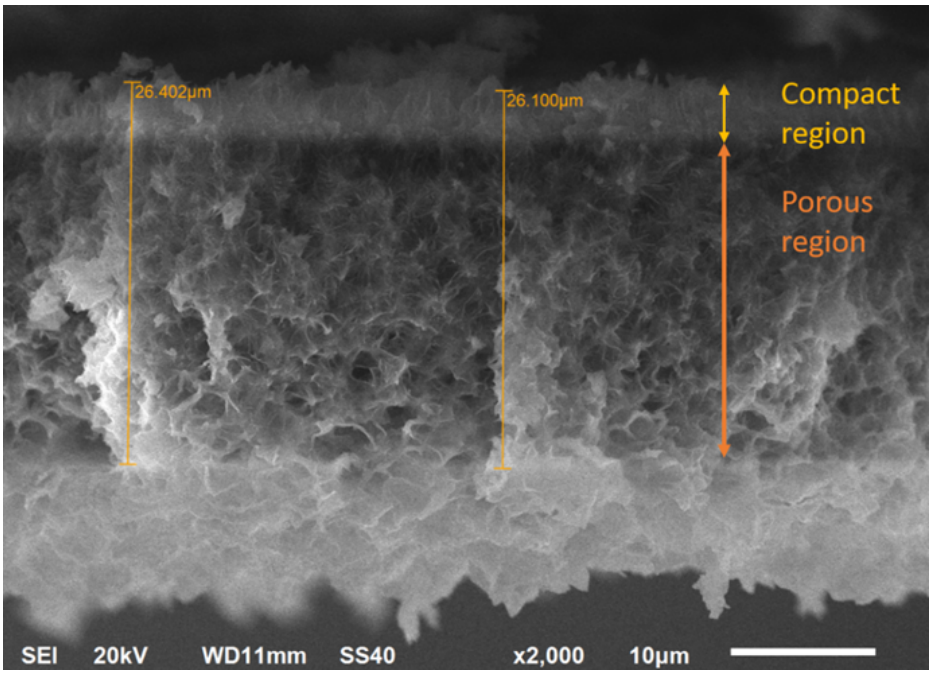

Figure 8. SEM image of the cross-section of a phosphate conversion coating synthesised at 15 mV s^{-1} for 20 cycles. The metal-coating interface is at the upper part of the image.

3.4. X-ray photoelectron spectroscopy

The SEM/EDX examination does not provide direct information on the Li^+ incorporation into the coating. For this reason, the XPS technique was employed to quantify the Li^+, Fe^{2+} and Fe^{3+} species present in the top layers of the coating. The analysis reported here focuses on samples prepared at 10 and 15 mV s^{-1} after 7 cycles. Two conditions were chosen: as prepared and after a polarisation at -0.7 V vs SCE (see Fig. 4) for 120 s. This last condition (denoted as CP in the following) corresponds to a slight cathodic polarisation aimed at promoting the reduction of Fe^{3+} and accordingly the incorporation of Li^+.

Fig. 9 shows the high resolution study of XPS spectra for samples prepared at 10 mV s^{-1}, for which the Li1s peak can be clearly deconvoluted at 59 eV [34]. Direct examination of the spectra in Fig. 9 reveals that the relative contribution of Li increases from the sample analysed just after preparation (Fig. 9a) to the sample after CP (Fig. 9b), thus proving the incorporation of Li^+ into the coating under CP.

The quantitative analysis is presented in Table 1 for the spectra in Fig. 9 (10 mV s^{-1}) and at 15 mV s^{-1} (spectra not shown). The data reveal that, as expected, the amount of Li^+ in the coating increases significantly after the cathodic polarisation, irrespective of the scan rate used for the coating formation.

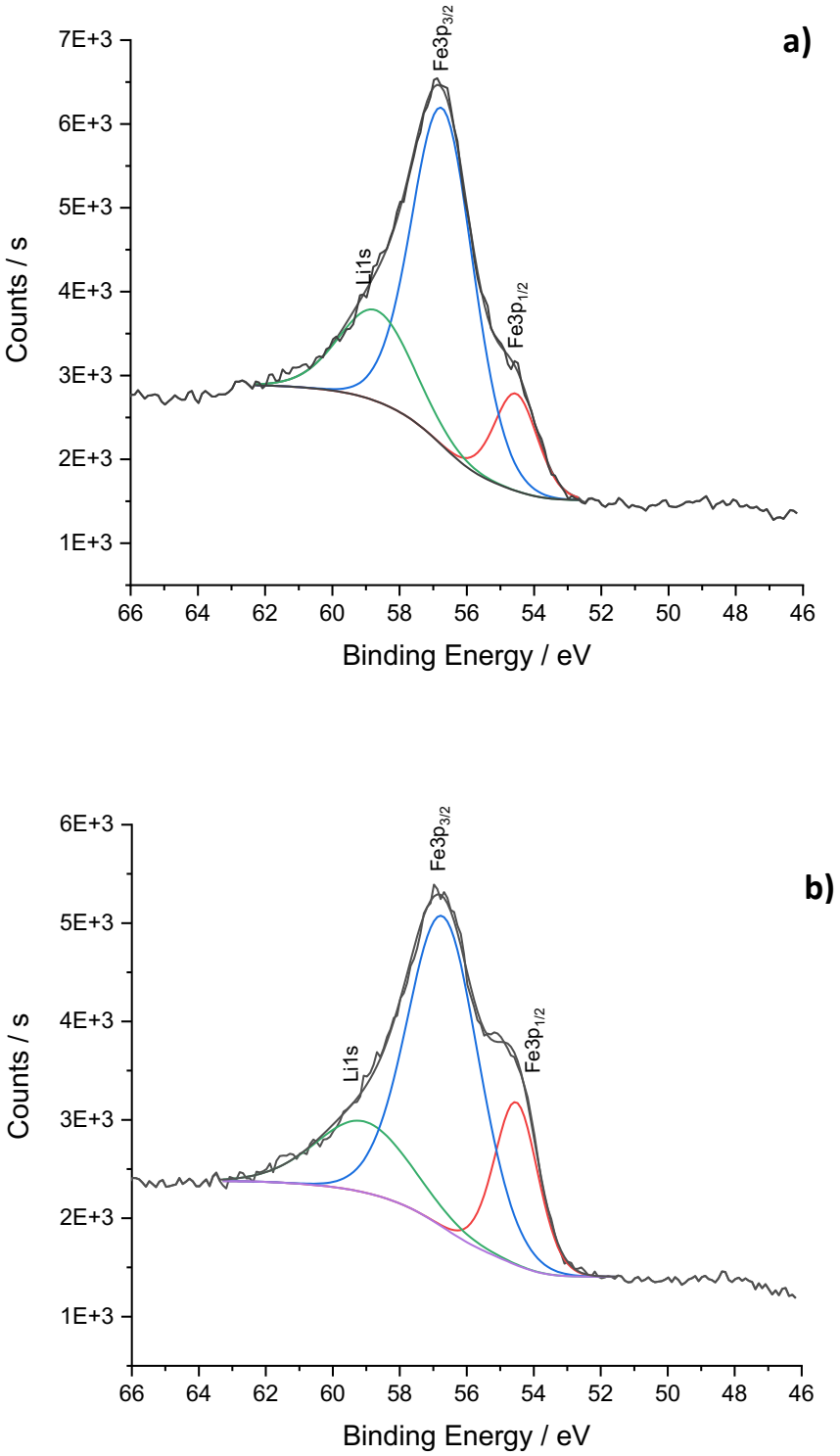

Figure 9. High resolution XPS spectra for Li1s and Fe3p with the corresponding deconvolutions for: **a)** a sample prepared at 10 mV s^{-1}; and **b)** a sample prepared at 10 mV s^{-1} + CP.

Table 1. Deconvolution of the high-resolution Li1s XPS signal for Li in the phosphate conversion layers formed at 10 and 15 mV s^{-1} (the spectra corresponding to 10 mV s^{-1} are presented in Fig. 9).

10 mV s^{-1}	10 mV s^{-1} + CP	15 mV s^{-1}	15 mV s^{-1} + CP
8.2%	12.6%	4.6%	12.3%

The quantification of the Fe^{2+} and Fe^{3+} is performed using the Fe2p signals (Fig. 10). According to the literature [35–37], the position of the $Fe2p_{3/2}$ and $Fe2p_{1/2}$ main peaks for Fe^{2+} in $LiFePO_4$ appear at binding energies of 709 and 722 eV, and satellites peaks are at 713 and 727 eV respectively. For Fe^{3+}, the main peaks for $FePO_4$ ($Fe2p_{3/2}$ and $Fe2p_{1/2}$) correspond to binding energies of 711 and 725 eV, respectively, whereas for $LiFePO_4$ these peaks shifted to 717 and 731 eV [38,39]. Moreover, it should be mentioned that the deconvolution of the whole spectra requires the contribution of Fe^0 signal at 707 and 720 eV.

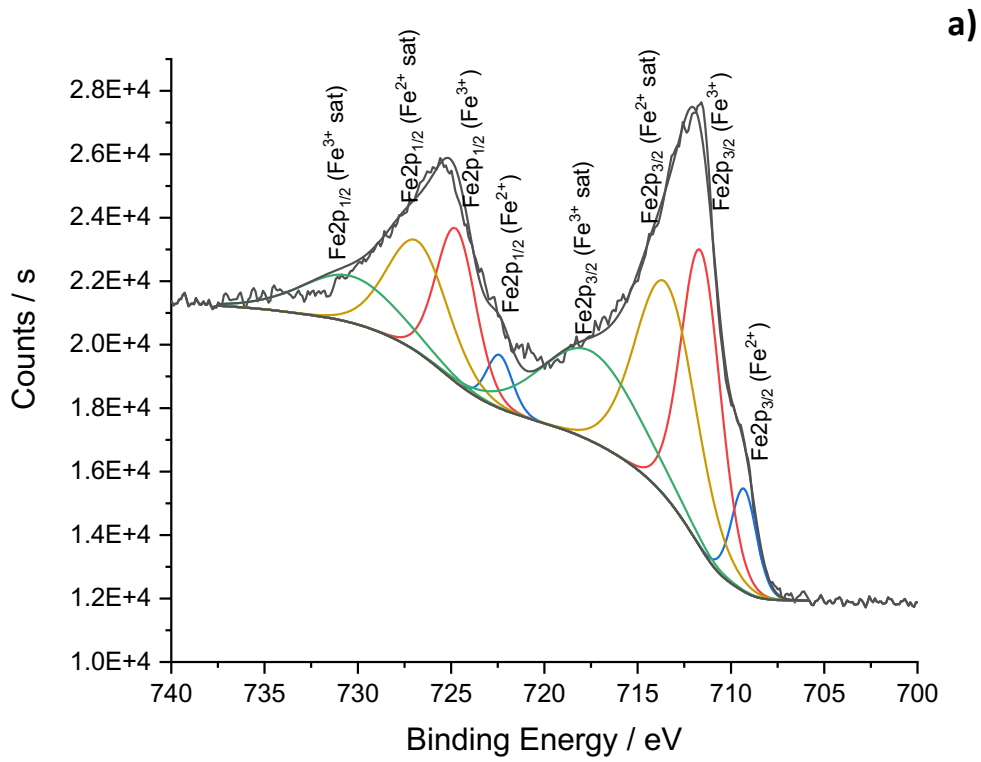

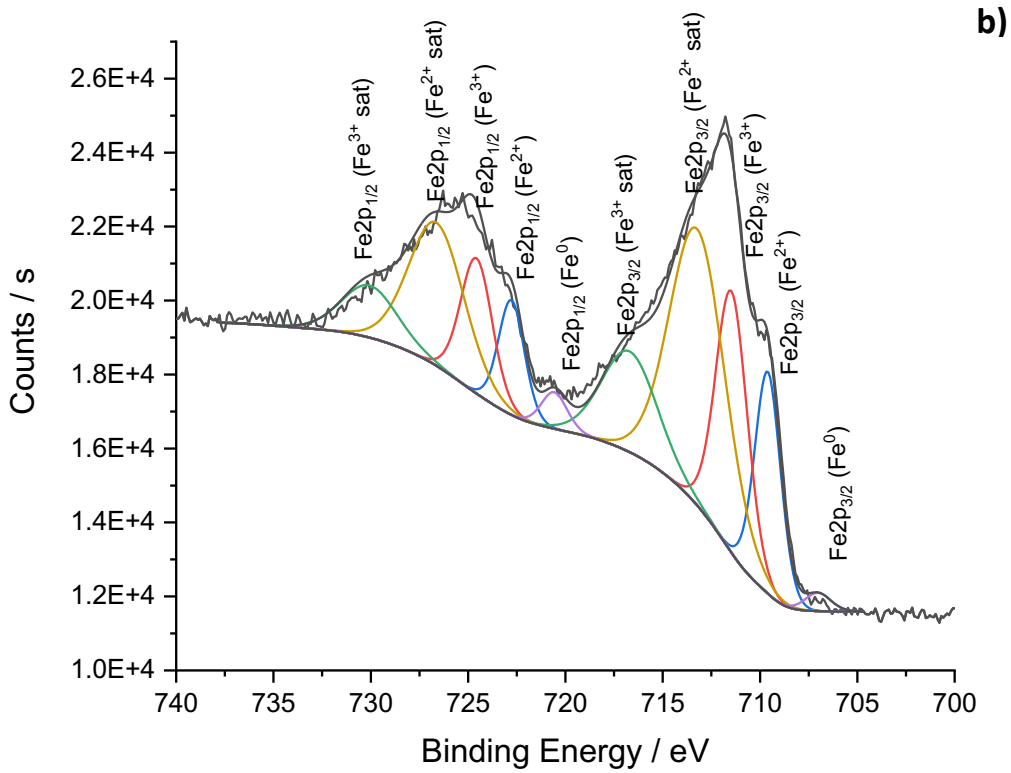

Figure 10. High resolution XPS spectra for Fe2p with the corresponding deconvolutions for: **a)** a sample prepared at 10 mV s^{-1}; and **b)** sample prepared at 10 mV s^{-1} + CP.

Visual examination of Fig. 10 reveals a remarkable increase in the Fe^{2+} peak at 709 eV between Fig. 10a (corresponding to the just–synthesised sample) and Fig. 10b (for the sample that has undergone CP). This fact agrees with the evolution of the Li1s peak presented in Figs. 9a and 9b, confirming that the increase of Li^{+} content in the coating is directly linked to the increase of Fe^{2+}.

The quantitative analysis is reported in Table 2 for the spectra presented in Fig. 10 (corresponding to 10 mV s^{-1}) and 15 mV s^{-1} (spectra not shown), showing that, as expected, the ratio Fe^{2+}/Fe^{3+} in the coating increases after the cathodic polarisation.

Table 2. Deconvolution of the high-resolution Fe2p XPS signal for Fe in the phosphate conversion layers formed at 10 mV s^{-1} (spectra in Fig. 10) and 15 mV s^{-1} (spectra not shown).

	10 mV s^{-1}	**10 mV s^{-1} + CP**	**15 mV s-1**	**15 mV s^{-1} + CP**
Fe^{2+}	32.0%	60.3%	38.3%	60.6%
Fe^{3+}	68.0%	39.7%	61.7%	39.4%
Fe^{2+}/Fe^{3+}	0.5	1.5	0.6	1.5

3.5. Scanning electrochemical microscopy

Chemical characterisation by SEM/EDX and XPS provides only "post-mortem" information about the composition of the grown coating. The SECM technique allows unique dynamic information to be obtained during the film formation and was used in this work in substrate generation / tip collector mode.

The SECM tip was located 50 μm from the iron surface to avoid any interference with the coating during its formation. Fig. 11 shows two independent experiments where the currents corresponding to the Fe^{2+} and Fe^{3+} species emitted from the substrate are monitored at the tip. Fig. 11a corresponds to the current for Fe^{2+} emission ($Fe^{2+} \rightarrow Fe^{3+} + e^-$, at fixed E_{tip}= + 0.6 V/ Ag/AgCl). It is worth noting that significant Fe^{2+} emission occurs from the beginning of the activation peak (at about -0.6 V/Ag/AgCl). This emission decays as the potential is swept towards the anodic direction, ascribed to the formation of the passive film. The Fe^{2+} emission is nearly null at -0.5 V/Ag/AgCl, indicating that all the current corresponding to the substrate oxidation is involved in the film formation.

An interesting feature in Fig. 11a is the shift observed between the currents of the substrate and the tip, which is an expected behaviour owing to the experimental configuration. Indeed, the probe is located 50 μm apart from the surface; the emitted species will need a certain amount of time (linked to their diffusion) to reach the tip [40]. This can be evaluated as τ in Eq. 1, where δ is the distance between tip and substrate, and *D* is the diffusion coefficient of the Fe^{2+} species.

$$\tau = \frac{\delta^2}{D} \qquad [1]$$

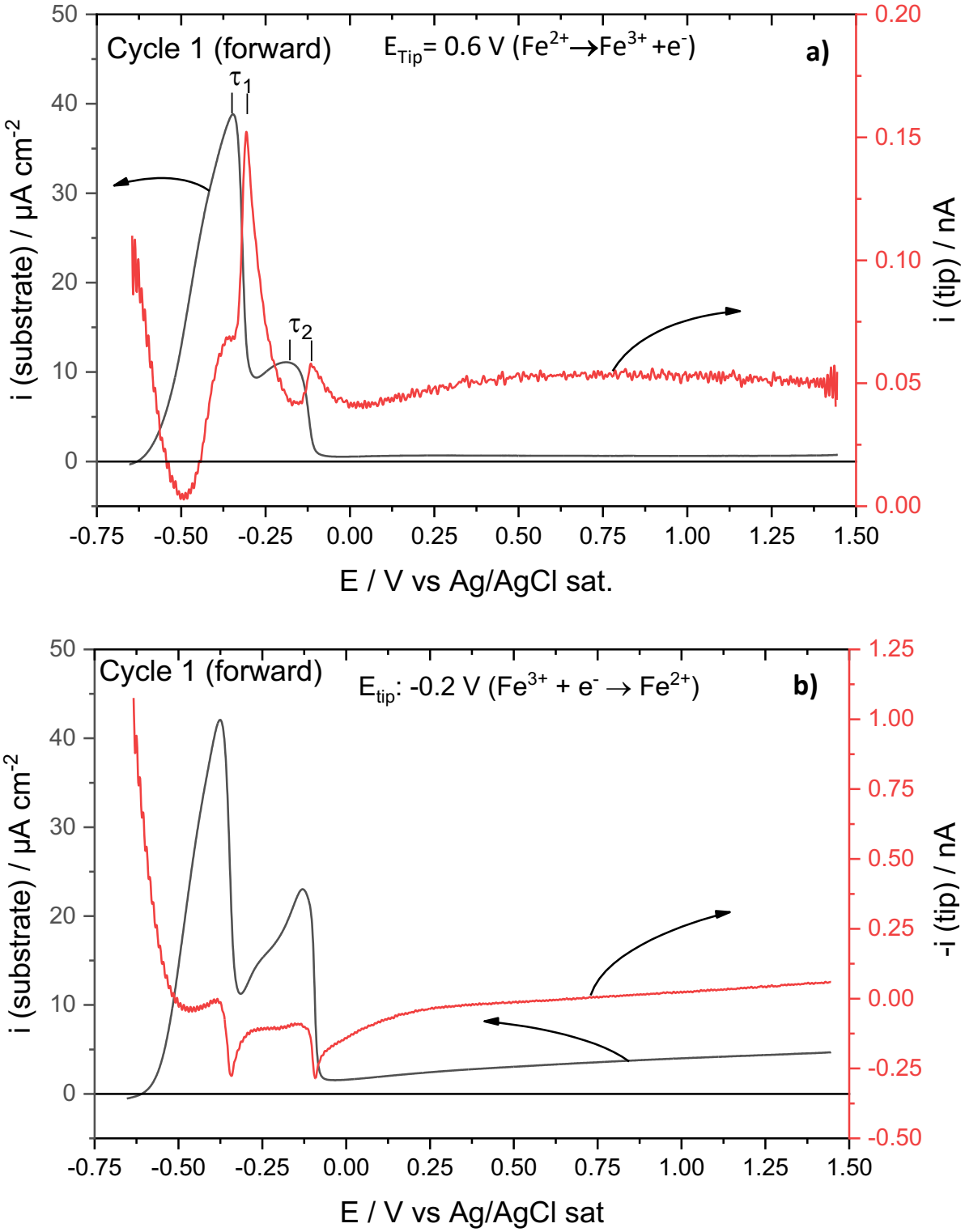

Figure 11. Forward (anodic) scans of the first cycle of cyclic voltammogram on the substrate at 10 mV s^{-1} and the corresponding currents at the SECM tip recorded at fixed potentials. **a)** $E_{SECM\ tip}$= +0.6 V/Ag/AgCl; and **b)** $E_{SECM\ tip}$= -0.2 V/Ag/AgCl.

The shifts denoted as τ_1 and τ_2 in Fig. 11a are τ_1= 4 s (40 mV in the Figure over 10 mV s^{-1} scan rate), and τ_2= 7 s (70 mV in the Figure over 10 mV s^{-1} scan rate). This is a surprising result because a priori, both travelling times should be equal, according to Eq. 1. Assuming a bare substrate surface, Eq. 1 provides D_1= 6 10^{-6} cm^2 s^{-1} as diffusion coefficient for the Fe^{2+} species emitted by the substrate. This value seems reasonable owing to the viscosity of the electrolyte. The fact that τ_2 is 3 s higher than τ_1 is more challenging to explain. A possible interpretation could be the formation of a top layer associated with the second activity peak. This aspect will be discussed later.

Figure 11b shows the emission of Fe^{3+} species. Interestingly, from the beginning of the experiment, significant Fe^{3+} emission occurs, simultaneous to that of Fe^{2+} (Fig. 11a), which means that a native oxide layer remains at the substrate surface after the cathodic treatment was performed. The persistence of the oxides layer on iron under cathodic polarisation has been reported elsewhere [40]. Later, the recorded Fe^{3+} current is almost null in the iron activity domain, with two peaks reaching positive current values. This can be attributed to ohmic coupling artefacts due to the two current drops of the substrate [25,26,41,42]. In the passive domain, the positive slopes of the substrate and tip currents are almost identical, indicating that the substrate dissolution occurs mainly via Fe^{3+} species, as expected [43].

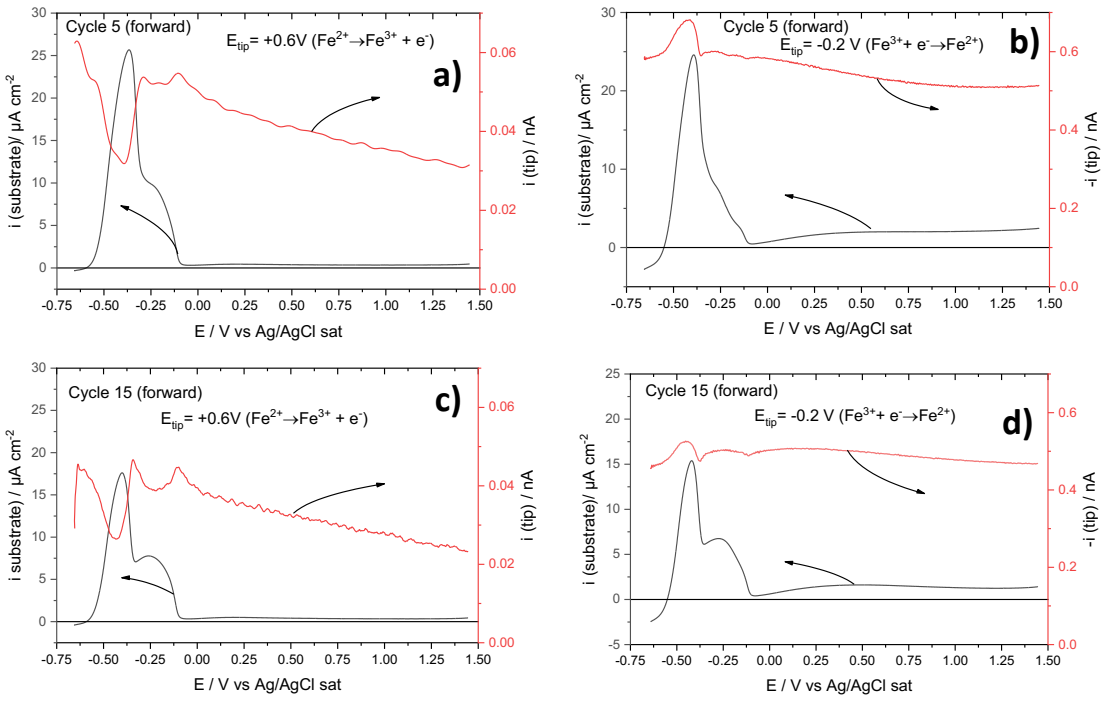

Figure 12. Forward (anodic) scans of the cyclic voltammograms on the substrate at 10 mV s^{-1} and the corresponding currents at the SECM tip at fixed potentials. **a)** 5th cycle on the substrate and $E_{SECM\ tip}$ = +0.6 V/Ag/AgCl. **b)** 5th cycle on the substrate and $E_{SECM\ tip}$ = -0.2 V/Ag/AgCl. **c)** 15th cycle on the substrate and $E_{SECM\ tip}$ = +0.6 V/Ag/AgCl. **d)** 15th cycle on the substrate and $E_{SECM\ tip}$ = -0.2 V/Ag/AgCl.

Figure 12 illustrates the release of the Fe^{2+} and Fe^{3+} in solution upon cycling monitored by the current at the tip. Both currents decrease as the number of cycles increases, which indicates a progressive surface blockage. The comparison of Fig. 12a with Fig. 12b, and Fig. 12c with Fig. 12d shows that the tip current associated with Fe^{3+} reduction is about one order of magnitude than that current corresponding to the Fe^{2+} oxidation, which points to some background process interfering with the Fe^{3+} reduction.

Interestingly, although τ_1 remains essentially constant at 4-5 s (as in Fig. 11a), τ_2 increases upon cycling until reaching 16 s after 15 cycles (Fig. 12c). Considering that after the 15th cycle, the coating reaches about 25 µm (Fig. 8), one can assume that of the 16 s, 5 s corresponds to the diffusion in solution and 11 s to the diffusion through the coating. Using Eq. 1, one gets $6\ 10^{-7}$ $cm^2\ s^{-1}$ for the value of the diffusion coefficient for Fe^{2+} species through the porous coating. This value is about one order of magnitude lower than the one obtained in solution, and seems a reasonable result associated with the porosity of the coating [44,45].

Moreover, Fig. 12 also shows the evolution of the Fe^{2+} and Fe^{3+} currents at the beginning of the potential sweeps (i.e., in the cathodic domain). The initial high emission rates (Figs. 11a and 11b, and Figs. 12a and 12b), attributed to chemical dissolution of the film, decreases over cycling (Figs. 12c and 12d). This can indicate a partial breakdown of the passive film under cathodic polarisation that decreases upon cycling as the coating develops. Such a non-homogeneous (or topotactic) development of the coating is compatible with the evolution of the Flade potential depicted in Fig. 2a: it tends to -0.1V/Ag/AgCl as the number of cycles increases.

4. Conclusions

Conversion coatings on iron substrate have been synthetised using cyclic voltammetry in a 2.85 M H_3PO_4 and 2.85 M LiOH electrolyte. The coatings developed efficiently exchange Li^+ ions with the aqueous environment, making them potential candidates for cathode materials in Li-ion batteries.

The SEM microscopy showed porous structures in agreement with EIS analysis in high–frequency, which demonstrates a porous electrode behaviour. After several cycles, the structures developed reached a steady state for Li^+ insertion/deinsertion, as shown with the subsequent CV curves. Moreover, the emission of Fe^{2+} and Fe^{3+} through the coating decreased upon cycling, as revealed by the SECM studies, which pointed to an increased barrier effect.

The porous nature of the conversion coatings makes them suitable for Li-ion batteries. They are also good candidates to accommodate corrosion inhibitors or lubricants, the traditional functionalities of phosphate coatings.

5. References

[1] N. Bretherton, G.E. Thompson, S. Turgoose, An electrochemical investigation of the development of phosphate conversion coatings, Corros. Sci. 35 (1993) 1297–1303. https://doi.org/10.1016/0010-938X(93)90351-G.

[2] J. Flis, J. Mańkowski, T. Zakroczymski, T. Bell, The formation of phosphate coatings on nitrided stainless steel, Corros. Sci. 43 (2001) 1711–1725. https://doi.org/10.1016/S0010-938X(00)00179-7.

[3] B. Díaz, L. Freire, M. Mojío, X.R. Nóvoa, Effect of carbon on the corrosion and wear performance of Zn-phosphate layers, Electrochim. Acta. 202 (2016) 299–309. https://doi.org/10.1016/j.electacta.2015.12.083.

[4] Y. Xie, M. Chen, D. Xie, L. Zhong, X. Zhang, A fast, low temperature zinc phosphate coating on steel accelerated by graphene oxide, Corros. Sci. 128 (2017) 1–8. https://doi.org/10.1016/j.corsci.2017.08.033.

[5] X. Zhang, G. Xiao, C. Jiang, B. Liu, N. Li, R. Zhu, Y. Lu, Influence of process parameters on microstructure and corrosion properties of hopeite coating on stainless steel, Corros. Sci. 94 (2015) 428–437. https://doi.org/10.1016/j.corsci.2015.02.021.

[6] S. Silva-Fernández, B. Díaz, I. Feijoo, X.R. Nóvoa, C. Pérez, Influence of pH and temperature in the performance of Zn phosphate conversion coatings, Electrochim. Acta. 457 (2023) 142510. https://doi.org/10.1016/j.electacta.2023.142510.

[7] J. Wang, X. Sun, Olivine LiFePO4: The remaining challenges for future energy storage, Energy Environ. Sci. 8 (2015) 1110–1138. https://doi.org/10.1039/c4ee04016c.

[8] M. Takahashi, H. Ohtsuka, K. Akuto, Y. Sakurai, Confirmation of long-term cyclability and high thermal stability of LiFePO4 in prismatic lithium ion cells, Proc. - Electrochem. Soc. PV 2003-28 (2004) 192–197. https://doi.org/10.1149/1.1874693.

[9] A.K. Padhi, K.S. Nanjundaswamy, J.B. Goodenough, Phospho-olivines as Positive-Electrode Materials for Rechargeable Lithium Batteries, J. Electrochem. Soc. 144 (1997) 1188–1194. https://doi.org/10.1149/1.1837571.

[10] J. Hu, W. Huang, L. Yang, F. Pan, Structure and performance of the LiFePO4 cathode material: from the bulk to the surface, Nanoscale. 12 (2020) 15036–15044. https://doi.org/10.1039/D0NR03776A.

[11] K. Zaghib, M. Dontigny, A. Guerfi, P. Charest, I. Rodrigues, A. Mauger, C.M. Julien, Safe and fast-charging Li-ion battery with long shelf life for power applications, J. Power Sources. 196 (2011) 3949–3954. https://doi.org/10.1016/j.jpowsour.2010.11.093.

[12] M.S. Whittingham, Lithium batteries and cathode materials, Chem. Rev. 104 (2004) 4271–4301. https://doi.org/10.1021/cr020731c.

[13] J.B. Goodenough, K.S. Park, The Li-ion rechargeable battery: A perspective, J. Am. Chem. Soc. 135 (2013) 1167–1176. https://doi.org/10.1021/ja3091438.

[14] X.G. Yang, T. Liu, C.Y. Wang, Thermally modulated lithium iron phosphate batteries for mass-market electric vehicles, Nat. Energy. 6 (2021) 176–185. https://doi.org/10.1038/s41560-020-00757-7.

[15] P.P. Prosini, Iron Phosphate Materials as Cathodes for Lithium Batteries, Springer London, London, 2011. https://doi.org/10.1007/978-0-85729-745-7.

[16] Y.Z. Dong, Y.M. Zhao, Y.H. Chen, Z.F. He, Q. Kuang, Optimized carbon-coated LiFePO4 cathode material for lithium-ion batteries, Mater. Chem. Phys. 115 (2009) 245–250. https://doi.org/10.1016/j.matchemphys.2008.11.063.

[17] F. Fathollahi, M. Javanbakht, H. Omidvar, M. Ghaemi, Improved electrochemical properties of LiFePO4/graphene cathode nanocomposite prepared by one-step hydrothermal method, J. Alloys Compd. 627 (2015) 146–152. https://doi.org/10.1016/j.jallcom.2014.12.025.

[18] E. Golestani, M. Javanbakht, H. Ghafarian-Zahmatkesh, H. Beydaghi, M. Ghaemi, Tartaric acid assisted carbonization of LiFePO4 synthesized through in situ hydrothermal process in aqueous glycerol solution, Electrochim. Acta. 259 (2018) 903–915. https://doi.org/10.1016/j.electacta.2017.10.123.

[19] T.V.S.L. Satyavani, A. Srinivas Kumar, P.S.V. Subba Rao, Methods of synthesis and performance improvement of lithium iron phosphate for high rate Li-ion batteries: A review, Eng. Sci. Technol. an Int. J. 19 (2016) 178–188. https://doi.org/10.1016/j.jestch.2015.06.002.

[20] D. Meng, H. Duan, S. Wu, X. Ren, S. Yuan, Lithium iron phosphate with high-rate capability synthesized through hydrothermal reaction in low Li concentration solution, J. Alloys Compd. 967 (2023) 171570. https://doi.org/10.1016/j.jallcom.2023.171570.

[21] Q. Cheng, X. Zhao, G. Yang, L. Mao, F. Liao, L. Chen, P. He, D. Pan, S. Chen, Recent advances of metal phosphates-based electrodes for high-performance metal ion batteries, Energy Storage Mater. 41 (2021) 842–882. https://doi.org/10.1016/j.ensm.2021.07.017.

[22] T. Wang, X. Wang, W. Lyv, X. Sun, J. Chen, E. Xu, K. Wu, Y. Zhang, Regeneration behavior of FePO4·2H2O from spent LiFePO4 under extremely acidic condition (pH < 0.8): Mechanism study and the properties of regenerated LiFePO4, Sep. Purif. Technol. 330 (2024) 125508. https://doi.org/10.1016/j.seppur.2023.125508.

[23] D.E. Stephenson, B.C. Walker, C.B. Skelton, E.P. Gorzkowski, D.J. Rowenhorst, D.R. Wheeler, Modeling 3D Microstructure and Ion Transport in Porous Li-Ion Battery Electrodes, J. Electrochem. Soc. 158 (2011) A781–A789. https://doi.org/10.1149/1.3579996.

[24] Q. Jing, J. Zhang, Y. Liu, C. Yang, B. Ma, Y. Chen, C. Wang, E-pH Diagrams for the Li-Fe-P-H2O System from 298 to 473 K: Thermodynamic Analysis and Application to the Wet Chemical Processes of the LiFePO4 Cathode Material, J. Phys. Chem. C. 123 (2019) 14207–14215. https://doi.org/10.1021/acs.jpcc.9b02074.

[25] J.J. Miksis, J. Newman, Primary Resistances for Ring-Disk Electrodes, J. Electrochem. Soc. 123 (1976) 1030–1036. https://doi.org/10.1149/1.2132986.

[26] C. Gabrielli, M. Keddam, H. Takenouti, Étude de la répartition du potentiel a la surface d'une électrode à disque-anneau, J. Chim. Phys. 69 (1972) 737–740. https://doi.org/10.1051/jcp/1972690737.

[27] F. Zucchi, G. Trabanelli, Anodic behaviour of Fe in phosphate solutions, Corros. Sci. 11 (1971) 141–151. https://doi.org/10.1016/S0010-938X(71)80090-2.

[28] C.V. D'Alkaine, P.C. Tulio, M.A.C. Berton, Quantitative Ohmic model for transient growths of passivating films, Electrochim. Acta. 49 (2004) 1989–1997. https://doi.org/10.1016/j.electacta.2003.12.029.

[29] J.R. Park, D.D. Macdonald, Impedance studies of the growth of porous magnetite films on carbon steel in high temperature aqueous systems, Corros. Sci. 23 (1983) 295–315. https://doi.org/10.1016/0010-938X(83)90063-X.

[30] B. Guitián, X.R. Nóvoa, A. Pintos, EIS as a Tool to Characterize Nanostructured Iron Fluoride Conversion Layers for Li-Ion Batteries, Bulg. Chem. Commun. 50 (2018) 82–89. http://bcc.bas.bg/BCC_Volumes/Volume_50_Special_D_2018/BCCvol50_SpecD_paper10.pdf.

[31] B. Guitián, S. Lascaud, X.R. Nóvoa, L. Ribeaucourt, E. Vidal, On the growth of nanostructured iron hydroxy-fluorides for Li-ion batteries, J. Power Sources. 241 (2013) 567–571. https://doi.org/10.1016/j.jpowsour.2013.04.145.

[32] E. Vidal, L. Ribeaucourt, X.R. Nóvoa, B. Guitián, Metal halide electrode with improved conductivity, and associated production method (EP3391441), EP3391441 EU patent WO 2017102424, 2018. https://www.google.com/patents/WO2017102424A1?cl=en.

[33] B. Díaz, L. Freire, M. Mojío, X.R. Nóvoa, Optimization of conversion coatings based on zinc phosphate on high strength steels, with enhanced barrier properties, J. Electroanal. Chem. 737 (2015) 174–183. https://doi.org/10.1016/j.jelechem.2014.06.035.

[34] C. Gao, J. Zhou, G. Liu, L. Wang, Lithium-ions diffusion kinetic in LiFePO4/carbon nanoparticles synthesized by microwave plasma chemical vapor deposition for lithium-ion batteries, Appl. Surf. Sci. 433 (2018) 35–44. https://doi.org/10.1016/j.apsusc.2017.10.034.

[35] G. Ji, J. Wang, Z. Liang, K. Jia, J. Ma, Z. Zhuang, G. Zhou, H.M. Cheng, Direct regeneration of degraded lithium-ion battery cathodes with a multifunctional organic lithium salt, Nat. Commun. 14 (2023) 1–11. https://doi.org/10.1038/s41467-023-36197-6.

[36] J.M. Deus, L. Freire, M.F. Montemor, X.R. Nóvoa, The corrosion potential of stainless steel rebars in concrete: Temperature effect, Corros. Sci. 65 (2012) 556–560. https://doi.org/10.1016/j.corsci.2012.09.001.

[37] W. Xiong, Q. Hu, S. Liu, A novel and accurate analytical method based on X-ray photoelectron spectroscopy for the quantitative detection of the lithium content in LiFePO4, Anal. Methods. 6 (2014) 5708–5711. https://doi.org/10.1039/c4ay00980k.

[38] R. Dedryvère, M. Maccario, L. Croguennec, F. Le Cras, C. Delmas, D. Gonbeau, X-Ray Photoelectron Spectroscopy Investigations of Carbon-Coated LixFePO4 Materials, Chem. Mater. 20 (2008) 7164–7170. https://doi.org/10.1021/cm801995p.

[39] L. Castro, R. Dedryvère, M. El Khalifi, P.E. Lippens, J. Bréger, C. Tessier, D. Gonbeau, The spin-polarized electronic structure of LiFePO4 and FePO 4 evidenced by in-lab XPS, J. Phys. Chem. C. 114 (2010) 17995–18000. https://doi.org/10.1021/jp106631v.

[40] F. Huet, M. Keddam, X.R. Nóvoa, H. Takenouti, Frequency and Time Resolved Measurements at Rotating Ring-Disk Electrodes for Studying Localized Corrosion, J. Electrochem. Soc. 140 (1993) 1955–1961. https://doi.org/10.1149/1.2220745.

[41] D. Trinh, M. Keddam, X.R. Novoa, V. Vivier, Alternating Current Measurements in Scanning Electrochemical Microscopy, Part 2: Detection of Adsorbates, ChemPhysChem. 12 (2011) 2177–2183. https://doi.org/10.1002/cphc.201001085.

[42] D. Trinh, M. Keddam, X.R. Novoa, V. Vivier, Alternating-Current Measurements in Scanning Electrochemical Microscopy, Part 1: Principle and Theory, ChemPhysChem. 12 (2011) 2169–2176. https://doi.org/10.1002/cphc.201001084.

[43] H.-H. Strehblow, Passivity of Metals Studied by Surface Analytical Methods, a Review, Electrochim. Acta. 212 (2016) 630–648. https://doi.org/10.1016/j.electacta.2016.06.170.

[44] B. Díaz, X.R. Nóvoa, B. Puga, V. Vivier, Macro and micro aspects of the transport of chlorides in cementitious membranes, Electrochim. Acta. 124 (2014) 61–68. https://doi.org/10.1016/j.electacta.2013.08.105.

[45] X.R. Nóvoa, C. Pérez, The use of smart coatings for metal corrosion control, Curr. Opin. Electrochem. 40 (2023) 101324. https://doi.org/10.1016/j.coelec.2023.101324.